

Disclaimer

This manuscript is under revision in Earth Science Reviews, and is not peer-reviewed.

Please feel free to contact any of the authors with feedback and suggestions for improvements.

Document history

Date	Action
08/Aug/2024	MS sent to co-authors for final draft acceptance Supplementary materials uploaded to Zenodo
12/Aug/2024	MS Submitted to EarthArXiv
15/Aug/2024	MS submitted to scientific journal for publication

RECONSTRUCTING PAST SEA-LEVEL CHANGES FROM STORM-BUILT BEACH RIDGES

PREPRINT, COMPILED AUGUST 12, 2024

Alessio Rovere ^{1,2*}, Marta Pappalardo³, Sebastian Richiano ⁴, Deirdre D. Ryan ³, Karla Rubio-Sandoval ²,
Patricio Martin Ruiz⁵, Alejandro Montes^{6,7}, and Evan J. Gowan ^{8,9}

¹DAIS, Department for environmental sciences, statistics and informatics, Ca' Foscari University of Venice, Venice, Italy

²MARUM, Center for Marine Environmental Sciences, University of Bremen, Bremen, Germany

³Department of Earth Sciences, University of Pisa, Pisa, Italy

⁴National Scientific and Technical Research Council, Instituto Patagónico de Geología y Paleontología, Puerto Madryn, Argentina

⁵Departamento de Geología, Universidad Nacional de la Patagonia San Juan Bosco, Comodoro Rivadavia, Chubut.

⁶CADIC-CONICET, Centro Austral de Investigaciones Científicas, Consejo Nacional de Investigaciones Científicas y Técnicas, Ushuaia, Argentina

⁷ICPA, Instituto de Ciencias Polares, Ambiente y Recursos Naturales, Universidad Nacional de Tierra del Fuego e Islas del Atlántico Sur, Ushuaia, Argentina

⁸Department of Earth and Environmental Sciences, Kumamoto University, Kumamoto, Japan

⁹KIKAI Institute for Coral Reef Sciences, Kagoshima, Japan

ABSTRACT

Storm-built beach ridges, built by waves on sedimentary coasts, can be used as geomorphological indicators of past sea level. However, quantifying the relationship between the geomorphological elements of the ridge and the paleo sea level at the time of deposition is difficult, as a beach ridge is primarily correlated to wave energy and only secondarily to the position of sea level. In this work, we propose a methodology to quantify the upper and lower limits of a storm-built beach ridge based on remote sensing data. We test our approach on a particularly well-preserved Pleistocene storm-built beach ridge in Patagonia, Argentina. Our results show that the paleo relative sea level reconstructed using remote sensing data coincides (87.6% similarity) with that obtained from measured modern analog landforms at the same location.

Keywords Pleistocene sea level · Beach ridges · Patagonia, Argentina · Paleo sea level

1 INTRODUCTION

Beach ridges are shore-parallel elongated mounds, occurring as single features or in sets, backing the coastline (Taylor and Stone, 1996; Hesp, 2006; Otvos, 2020) and formed by coastal processes. Different types of beach ridges have been described, categorized based on morphological and sedimentological features (Otvos, 2020). They are considered as originally being deposited by swash during high or low wave-energy conditions, but some models account for their genesis as the product of aggradation of an offshore bar. Regardless the typology, all beach ridges are considered as progradational features.

Storm-built beach ridges on sedimentary coasts are created by the accumulation of sediments by waves above sea level (Tamura, 2012). The observation of beach ridges (that Charles Lyell defined "shingle beaches in his "Principles of Geology, Lyell, 1837), and their use as proxies for the past position of relative sea level (RSL, that is local sea level uncorrected for vertical land motions), dates back at least to Charles Darwin who, on his voyage through South America, described several beach ridges with embedded shells and discussed their relationship with past positions of the shoreline (Darwin, 1846).

While coastal landforms (such as beach ridges) can be described with classic geologic methods, quantifying their relationship with a former sea level requires rigorous approaches, that have been employed since the mid-80s (Van de Plassche 2013, first edited in 1986, and Shennan, 1986). Recently, the "Handbook of sea-level research" by Shennan (2015) has collected the main methods that are currently used to study former sea-level

changes, which have been since then successfully used to build global sea-level databases for different time periods (Khan et al., 2019; Rovere et al., 2023). One key concept is that a geomorphological feature can be considered a sea-level index point if three key properties are known: i) its position and elevation measured with the highest possible accuracy; ii) its age of formation; iii) its relationship with sea level at the time of its formation. This relationship is called the "indicative meaning" (Shennan, 1986).

The indicative meaning is composed by two numerical values. The indicative range (IR) represents the vertical elevation range occupied by a sea-level index point, relative to contemporary tidal datums. The reference water level (RWL) is the distance between the midpoint of the IR and the former tidal datum, and represents the elevational difference between the sea-level index point and the former sea-level (expressed as a former tidal datum, such as Mean Sea Level). The best way to quantify the indicative meaning of a sea-level index point is to measure a modern analog and apply the elevation offset (and associated uncertainty) between the modern sea-level and the modern feature to the paleo context (Shennan, 2015).

Several authors have used storm-built beach ridges as paleo sea-level index points, in particular along the Atlantic coasts of Argentina and Uruguay (e.g. Rostami et al., 2000; Schellmann and Radtke, 2000; Zanchetta et al., 2012; Martínez and Rojas, 2013; Pappalardo et al., 2015). However, modern analogs for these landforms have been seldom described, making literature-based compilations of sea-level data (Gowan et al., 2021) more challenging than in other areas. In this work, we propose a method

57 to establish the indicative meaning of storm-built beach ridges
 58 using remote sensing data. The method stems from recent works
 59 and definitions (Lorscheid and Rovere, 2019; Rubio-Sandoval
 60 et al., 2024), and is based on modern wave and tidal data, and
 61 wave runup models. We use as a benchmark for our method a
 62 site in central Patagonia, Argentina (south of the town of Caleta
 63 Olivia, Santa Cruz Province), where both the modern analog and
 64 fossil stratigraphy are clearly defined, and have been constrained
 65 by field surveys.

66 2 BENCHMARK SITE

67 The site we use to benchmark our methodology (46°33'29.0" S,
 68 67°25'59.9" W, hereafter called "benchmark site") is located
 69 within a quarry site locally named "Cantera Delgado", ~15 km
 70 south of the town of Caleta Olivia, in the central part of the
 71 San Jorge Gulf, ~1500 km south of Buenos Aires (Figure 1). In
 72 general, this area is located on a passive margin and is embed-
 73 ded within the South America Plate. Caleta Olivia is located
 74 along the central-southern coast of the Gulf of San Jorge, an
 75 intracratonic, extensional basin formed since the Mid- Jurassic
 76 between the two North Patagonian and Deseado Massifs (Ramos
 77 and Ghiglione, 2008).

78 In this area, several authors reported Holocene and Pleistocene
 79 beach ridges, that reach elevations of 10-20 meters above modern
 80 sea level (e.g., Codignotto, 1983; Codignotto et al., 1992;
 81 Schellmann, 1998; Rostami et al., 2000; Aguirre, 2003; Schell-
 82 mann and Radtke, 2003; Ribolini et al., 2014; Richiano et al.,
 83 2021). Although the amount of literature on this site and the sur-
 84 rounding area is remarkable, so far there is no agreement on the
 85 interpretation of the beach ridges extensively occurring in this
 86 area as paleo-sea-level indicators. In fact, there is no correlation
 87 between their height and age, and in many cases the same height
 88 corresponds to different ages (e.g. Pleistocene/Holocene).

89 2.1 Survey methods

90 We used differential Global Navigation Satellite systems (GNSS)
 91 to measure the position and elevation of the modern beach pro-
 92 file (Figure 2 B) and the fossil beach ridge (Figure 2 C). We
 93 employed a single-band EMLID RS+ GNSS composed of a base
 94 and a rover unit communicating via radio. The base station was
 95 located in full view of the sky and was left static collecting data
 96 for ~2h and 42 minutes. The data collected from the base station
 97 were processed using the Precise Point Positioning service of
 98 the Natural Resources of Canada (NRCAN-PPP). This allowed
 99 gathering a corrected base position, which was then used to
 100 correct each rover point using the scripts available in Rovere
 101 (2021).

102 Data were originally recorded in WGS84 coordinates, with
 103 height above the ITRF2008 ellipsoid. Orthometric heights
 104 (above mean sea level) were then calculated subtracting the
 105 GEOIDEAR16 geoid height from the measured ellipsoid height.
 106 It was estimated that the GEOIDEAR16 has an overall vertical
 107 accuracy of 0.1 m (Piñón et al., 2018). It is worth noting that
 108 Pappalardo et al. (2019) surmised that in some areas of Patago-
 109 nia, referring GNSS data to the GEOIDEAR16 geoid might be
 110 affected by large discrepancies if compared with the sea level
 111 datum obtained by tide gauge data. We remark that such discrep-
 112 ancy would not affect our results, as in the following sections

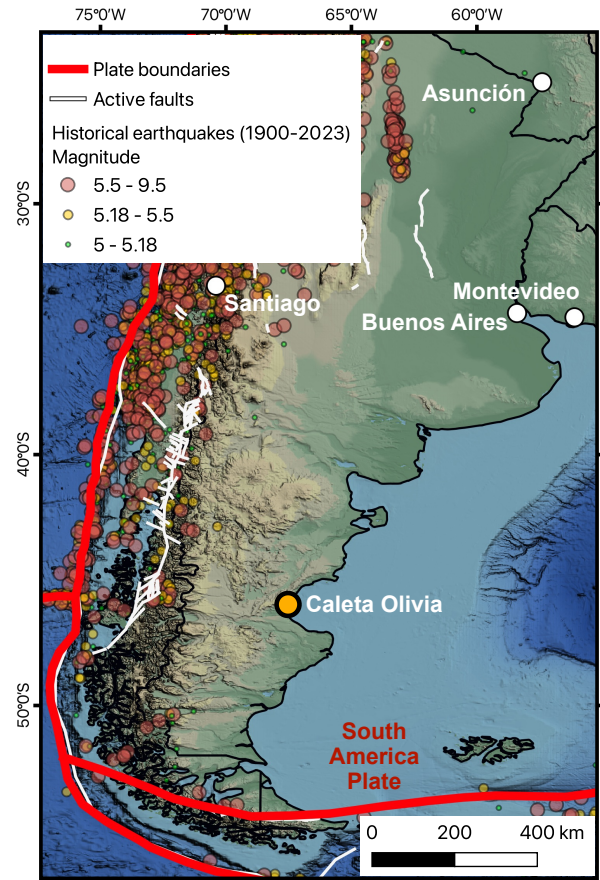


Figure 1: **Study area.** Location of the town of Caleta Olivia (the benchmark site is 15 km south of the town) within the Southern part of South America. Credits: Base map from Ryan et al. (2009). Active faults from Styron (2019) and plate boundaries derived from Bird (2003), as modified by Hugo Ahlenius and Nordpil on GitHub (<https://github.com/fraxen/tectonicplates>). Historical earthquakes from the US Geological Survey (2017).

113 we only compare elevation within this site, hence is it only rele-
 114 vant that the same elevation datum is used. However, we make
 115 available all the GNSS data collected in this work, that are origi-
 116 nally referred to the ITRF2008 ellipsoid (see Supplementary
 117 Information for details).

118 The elevation error (σE) of each GNSS point surveyed in the
 119 field was calculated using the following formula:

$$120 \sigma E = \sqrt{GNSS_e^2 + Base_e^2 + Geoid_e^2} \quad (1)$$

121 Where $GNSS_e$ is the error given as output by the GNSS system,
 122 $Base_e$ (only for data collected with the Base-Rover EMLID
 123 GNSS) is the elevation error of the base station, and $Geoid_e$
 124 is the error associated with the GEOIDEAR16 (0.1 m). Overall,
 125 the 1σ elevation error associated to our measurements is 0.30
 126 m.

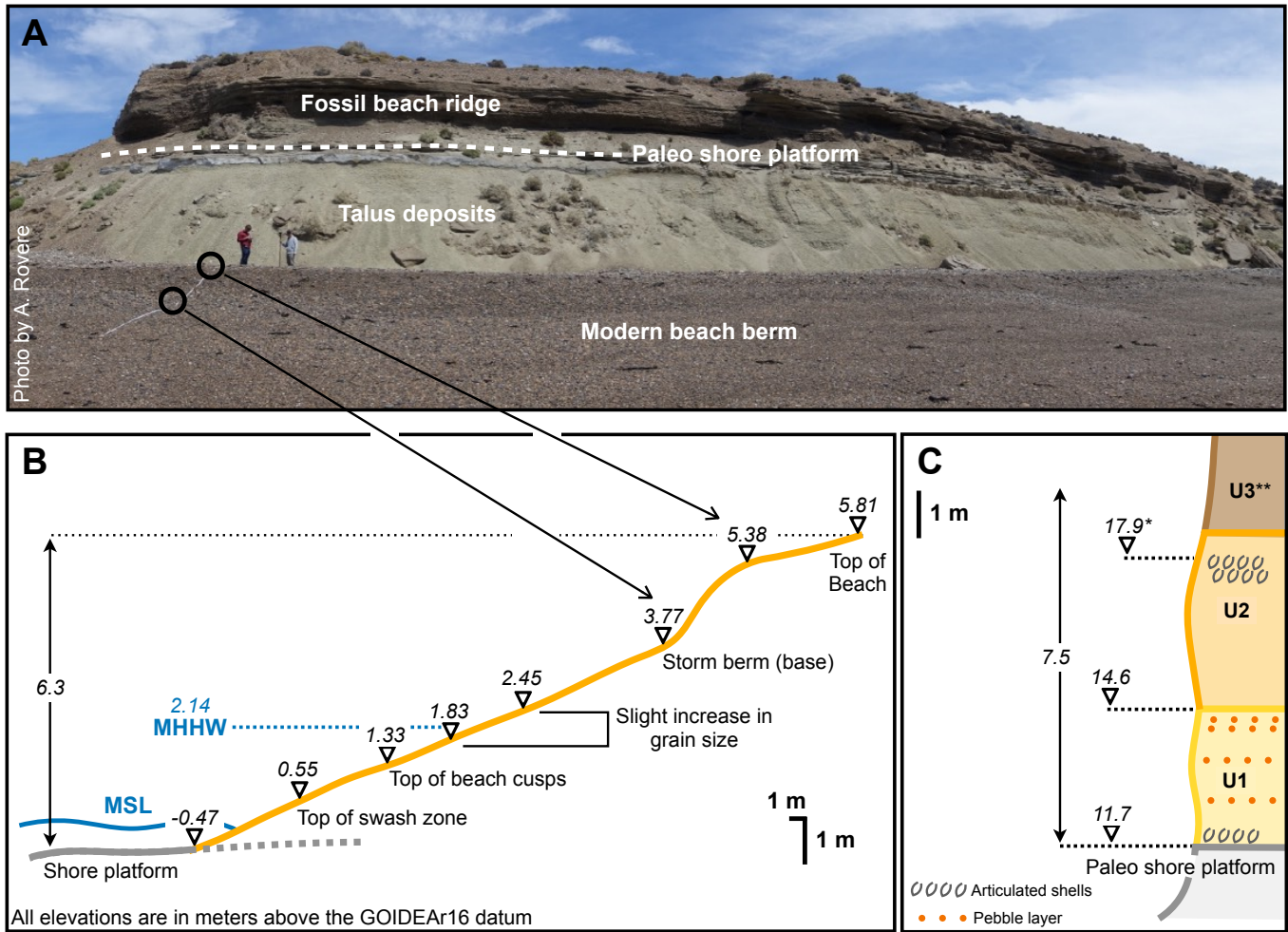


Figure 2: A) Composite photograph showing the modern beach berm (in the foreground) and the fossil beach ridge (in the background) at the benchmark site. B) GNSS profile of the modern beach with distinctive geomorphological elements. MSL = Mean Sea Level; MHHW = Mean Higher High Water. C) Stratigraphic section of the fossil (Pleistocene) beach ridge, divided into two units (U1 and U2). * indicates an elevation taken ~15 meters south of the section, as the point was not accessible on the vertical beach ridge face. ** Unit 3 was recognised at this section, but is more complete a few hundred meters from this section, and was described by Ribolini et al. (2014) starting at ~17m above sea level.

126 2.2 Modern beach

127 The modern beach at our benchmark site (Figure 2 A,B) lies upon a shore platform, carved into the sedimentary rocks of the Monte León formation (which a few kilometers north, in the Chubut Province, is called Chenque formation) (Upper Oligocene / Lower Miocene, Martínez et al., 2020). Abrasion and subordinately bioerosion are apparently the main processes shaping this platform (Supplementary Figure 1) The shore platform can be observed at low tide (Supplementary Figure 1 B,C), and the contact with the beach deposits was measured at -0.47 m. The modern beach is characterized by beach cusps, at an elevation of 1.33 m. The grain size is between coarse gravels to pebbles, and there is a slight increase in grain size between the elevation of 1.83 and 2.45 m, which correspond to Mean Higher High Water (MHHW, 2.14 m, see 4.2.1 for calculation of this tidal datum). Above this level, a well-defined storm berm is a prominent geomorphological feature between 3.77 and 5.81 m.

143 The modern storm berm appears laterally continuous, and at this location covers a ca. 1.5 m high cliff carved in an Holocene marine terrace which is clearly visible all along the coast N and S of the benchmark site (Ribolini et al., 2014). The beach deposits are covered by talus deposits created by quarried materials at 5.81 m. 144 145 146 147 148

149 2.3 Pleistocene storm-built beach ridge

150 The talus deposits covering the upper part of the modern beach have a resting angle of 30°- 40°(Figure 2 A), and are about 5m high. At ~10 m above sea level, the Monte León formation outcrops again. Here, it is cut by paleo marine abrasion, forming a fossil shore platform overlain by two sedimentary units with different characteristics. Unit 1 develops from 11.7 to 14.6 m in elevation (Figure 2 C, Supplementary Figure 2 A). At the base of this unit, very close to the contact with the shore platform, there are mollusk shells of the species *Ameghinomya antiqua* 151 152 153 154 155 156 157 158

159 (formerly *Protothaca antiqua*) articulated but not in living po-
 160 sition (Supplementary Figure 2 D). Unit 1 is composed by fine
 161 sands, interbedded by decimeter-wide layers characterized by
 162 coarser sediments (pebbles and gravels, Supplementary Figure 2
 163 E). Towards the upper part of Unit 1, the coarser layers become
 164 more frequent up to the transition with Unit 2 (Supplementary
 165 Figure 2 C) and contain fragmented and disarticulated whole
 166 valves of *Ameghinomya antiqua*, as well as articulated valves.
 167 Unit 2 develops between 14.6 and ~18 m in elevation, and is
 168 characterized by an alternation of pebbles and gravels (Supple-
 169 mentary Figure 2 B) and by the presence, at its top, of a layer
 170 with articulated shells of *Ameghinomya antiqua*, not in living
 171 position.

172 A further unit (Unit 3), reaching up to 20.6 m, rests on top of
 173 Unit 2. This is a complex continental unit, described by Ribolini
 174 et al. (2014) a few hundred meters from the section reported in
 175 this paper, still within "Cantera Delgado". Its bottom part is rep-
 176 resented by silty sand with scattered pebbles displaying multiple
 177 pedogenetic carbonate crusts and incised by periglacial features
 178 (sand wedges). An aeolian sand cover seals the sequence. The
 179 formation of this continental unit was dated by Ribolini et al.
 180 (2014) to a time span encompassing the Last Glacial Maximum.

181 The location of our benchmark site coincides with that reported
 182 by Schellmann (1998) for samples Pa 124 to 126 (both *Ameghi-*
 183 *nomya antiqua* shells), that these authors collected between 16.5
 184 and 18 meters above mean sea level (possibly within Unit 2
 185 described here). Six replicates of these samples were dated using
 186 Electron Spin Resonance, yielding ages ranging from 172 ± 15
 187 ka to 212 ± 26 ka (hence consistent with Marine Isotopic Stage 7,
 188 Schellmann, 1998). Shells of the same species, were sampled
 189 by Schellmann (1998) at two other sites (Pa 70 and Pa 71), lo-
 190 cated 5.5 to 6.5 kilometers south of our benchmark site from
 191 horizons at ~10 and ~15 meters above sea level (Schellmann,
 192 1998). These yielded ages consistent with Marine Isotopic Stage
 193 (MIS) 5e (~125 ka). In the same general area, at a site called
 194 "Bahia Langara" Rostami et al. (2000) obtained U-series ages
 195 consistent with MIS 5e at 16-17 m and with MIS 7 at 14 m above
 196 sea level (no vertical datum reported, assumed above mean sea
 197 level). A definitive age attribution for this site is out of the scope
 198 of this work, however these data confirm that the beach ridge
 199 we surveyed at the benchmark site is Pleistocene (either MIS 5e
 200 or MIS 7) in age.

201 3 PALEO RSL FROM MODERN ANALOG

202 The storm beach ridge exposure at the benchmark site is a rare
 203 occurrence, at least within the Patagonian context (Blanco-Chao
 204 et al., 2014). In fact, quarrying works in "Cantera Delgado"
 205 produced a clear-cut section across its face, exposing the com-
 206 plete beach ridge sequence, from the shore platform up to the
 207 highest deposits. At most other locations only parts of the beach
 208 ridge (usually the upper parts, showing articulated shells as those
 209 in U2, Figure 2) are exposed. The advantage of this peculiar
 210 exposure is that it is possible to better evaluate the indicative
 211 meaning of the beach ridge, and give a robust quantification of
 212 RSL at this site. This is one of the few places along the Atlantic
 213 coast of Patagonia where a shore platform outcrops beneath the
 214 beach (Blanco-Chao et al., 2014), providing the possibility to
 215 use it as a modern analog for paleo sea-level reconstructions.



Figure 3: Accumulation of articulated and disarticulated mollusk shells (white among the gray gravel sands) on the modern beach at Mazarredo, ~80 km south of the benchmark site.

216 The geomorphological element of Patagonian beach ridges that
 217 is often correlated to paleo sea level is a layer embedded within
 218 coarse gravels or pebbles composing the ridge, characterized by
 219 articulated shells of *Ameghinomya antiqua*. At the benchmark
 220 site, this layer is embedded within Unit 2 at 17.9 m above mod-
 221 ern sea level (Figure 2 C). While in the study area at the time
 222 of survey we could not observe a modern analog shelly deposit
 223 on the ridge, in the regional context similar accumulations of
 224 articulated shells are observed between the ordinary berm (or the
 225 swash zone of ordinary waves) and the storm berm (Figure 3).
 226 In our modern beach profile, the top of the swash zone can be
 227 approximated by the top of beach cusps (1.33 m) and the top of
 228 the storm berm (5.38 m). Applying these two values of upper
 229 and lower limits of the indicative range, we estimate that paleo
 230 RSL at the time of formation of the beach ridge was 14.5 ± 2 m,
 231 1σ .

232 The occurrence in the benchmark site of both the modern and
 233 a paleo shore platform, the latter outcropping underneath the
 234 Pleistocene storm-built beach ridge, provides a further possibil-
 235 ity to calculate paleo RSL. This can be done accepting a number
 236 of approximations. In macrotidal and high-energy environments,
 237 similar shore platforms are often considered as intertidal features
 238 (Sunamura, 1992).

239 We assume that the elevation at which the paleo shore platform
 240 was measured (11.7 m, Figure 2 C) was originally located be-
 241 tween mean sea level and Mean Lower Low Water (MLLW),
 242 corresponding to the shore platform outer edge. This could be
 243 an overestimation if the seaward portion of the former shore
 244 platform had been extensively eroded by the Holocene RSL
 245 transgression. The presence of the Holocene terrace under-
 246 neath the modern storm berm (reported in Ribolini et al., 2014),
 247 though, suggests that this was not the case. Consequently, the

248 the upper and lower limits of the indicative range are assumed to
 249 be respectively Mean Sea Level (MSL) and MLLW. Their current
 250 position can be calculated assuming that the point measured
 251 at -0.47 broadly corresponds to the shore platform inner edge
 252 (Figure 2 B) and using 4.28 as the tidal range. Paleo RSL at the
 253 time of the shore platform formation was 15.4 ± 1.1 m, 1σ .

254 4 PALEO RSL FROM RUNUP MODELS

255 While the most reliable methodology to calculate paleo RSL is
 256 the one outlined in the previous section, stemming from data
 257 and interpretation of the modern analog, this kind of information
 258 is not always available. For example, most of the data reviewed
 259 within in the World Atlas of Last Interglacial shorelines (Rovere
 260 et al., 2023), including a recent review of Argentinian beach
 261 ridges (Gowan et al., 2021), make use of IMCalc (Lorscheid and
 262 Rovere, 2019), a tool that allows to give a first-order quantifica-
 263 tion of the indicative meaning based on wave and tidal data in
 264 absence of data on modern analogs.

265 4.1 Previous works

266 For storm beach ridges, IMCalc uses the formula of Stockdon
 267 et al. (2006) to calculate the wave runup exceeded by 2% of the
 268 waves (R_2) at high tide (MHHW) in fair weather and storm wave
 269 conditions, and equating them to the elevation of, respectively,
 270 the ordinary and storm berm on an ideal beach profile, with a
 271 general slope (β) of 0.08. The significant wave height and period
 272 are extracted from wave data from the CAWCR (Collaboration
 273 for Australian Weather and Climate Research) wave hindcast
 274 (Durrant et al., 2013), which is based on the NOAA WaveWatch
 275 III wave model (Tolman et al., 2009) and the NCEP CFSR
 276 surface winds and sea ice data (Saha et al., 2010). For fair
 277 weather conditions, IMCalc uses average wave height and period,
 278 while for storm conditions, it uses the upper 2σ significant wave
 279 height and period. Using the IMCalc tool to calculate paleo RSL
 280 from the layer of articulated shells within Unit 2 (at 17.9 m), we
 281 obtain the a paleo RSL value of 15.9 ± 0.7 m (1σ).

282 Rubio-Sandoval et al. (2024) suggests a more detailed approach
 283 than IMCalc, that employs wave data measured by satellite alti-
 284 metry and analysed with the RADWave software (Smith et al.,
 285 2020). This is a python package that provides access to altimeter
 286 datasets using the Australian Ocean Data Network (AODN)
 287 database, that contains data spanning from 1985 to present, val-
 288 idated and calibrated by Ribal and Young (2019). Wave data
 289 for the period Jan 2000 - Jan 2023 (Supplementary Figure 3)
 290 were then employed in a runup model ensemble implemented
 291 in the *py-wave-runup* tool (Leaman et al., 2020), also account-
 292 ing for tides extracted from the FES2014 global tidal model
 293 (Lyard et al., 2021; Carrere et al., 2016). The beach slope was
 294 obtained with the CoastSat.Slope (Vos et al., 2020) tool. With
 295 this approach, we calculate that the upper limit of the indicative
 296 range for beach ridges at the benchmark site is 0.91 m, while
 297 the lower limit is 3.51 m (Supplementary Figure 3 B). Applying
 298 this range to the elevation of articulated shells of Unit 2 (17.9
 299 m), we calculate that paleo RSL is 15.7 ± 1.3 m (1σ).

300 4.2 Runup calculation workflow

301 Here, we build on the concept idealised in IMCalc and on the
 302 approach of Rubio-Sandoval et al. (2024) described above to

303 build a workflow that allows calculating the indicative meaning
 304 for a beach ridge using the best datasets and tools available. We
 305 validate the results with the paleo RSL obtained at the bench-
 306 mark site described above. The workflow is implemented in
 307 python and is divided in three steps, described below. Each
 308 step can be reproduced in other areas via the jupyter notebooks
 309 supporting this paper (Rovere, 2024).

310 4.2.1 Step 1 - Tide and wave data

311 In this first step, we retrieve tidal and wave data from global
 312 datasets. Water level data over the period 01 Jan 1993 to 01 Jan
 313 2023 (30 years) was calculated using the FES2014 global tidal
 314 model (Lyard et al., 2021; Carrere et al., 2016) at a point slightly
 315 offshore of the benchmark site (Figure 4 A). Using these data as
 316 input to the "CO-OPS Tidal Analysis DatumCalculator" (Licate
 317 et al., 2017) we calculate that MHHW is 2.14m and MLLW is -
 318 2.14m (Figure 4 B).

319 Wave data is retrieved from the Copernicus Marine Environment
 320 Monitoring Service (CMEMS) WAVEReanalYSIS (WAVERYS,
 321 Law-Chune et al., 2021), which is driven by the ERA5 10-m
 322 wind and sea ice fraction, as well as GLORYS12 oceanic
 323 currents (Lellouche et al., 2018). Also wave data are retrieved
 324 for a period of 30 years (01 Jan 1993 to 01 Jan 2023), slightly
 325 offshore our benchmark site (Figure 4 A). In our area of interest,
 326 the waves directed towards the coast (with direction NE to SE)
 327 have a median significant wave height of 1.2 m and median
 328 significant wave period of 9 s (Figure 4 C,D), with main direction
 329 of waves from NNE (Figure 4 E,F).

330 4.2.2 Step 2 - Beach slope

331 Determining the beach slope (β) is a simple operation, that can
 332 be performed on any beach with basic topographic methods.
 333 At our benchmark site (Figure 2 B), it can be determined by
 334 dividing the difference between the base of the storm berm (3.77
 335 m) and the top of swash zone (0.55 m) by the distance between
 336 the two (30.5 m). With this operation, we can determine that β
 337 is 0.1.

338 If no modern analog data is available, calculating β becomes
 339 more difficult. It is possible to do it via satellite-derived shore-
 340 lines with CoastSat.Slope (Vos et al., 2020), a tool implemented
 341 within the CoastSat software (Vos et al., 2019). Thanks to this
 342 software, we could download 350 satellite images from Landsat
 343 7,8,9 and Sentinel 2, spanning from August 2000 to December
 344 2023 (see an example in Figure 5 A). Over a coastal stretch of
 345 ~ 2 km around our study site, we identified 5 transects, where we
 346 evaluated coastal evolution over the period of available imagery,
 347 and extracted the beach slope.

348 The results show that this beach, at the net of seasonal variations,
 349 has been rather stable throughout the last 23 years (Figure 5 B).
 350 This is an important point, as it strengthens the assumption that
 351 the modern beach and the modern beach slope are representative
 352 of a steady-state, hence they are more representative of long-
 353 term conditions of this beach. From CoastSat.Slope, we obtain
 354 that the average β over the five transects is 0.1, which coincides
 355 with what we measured in the field. This slope will be used in
 356 the calculations of runup described below.

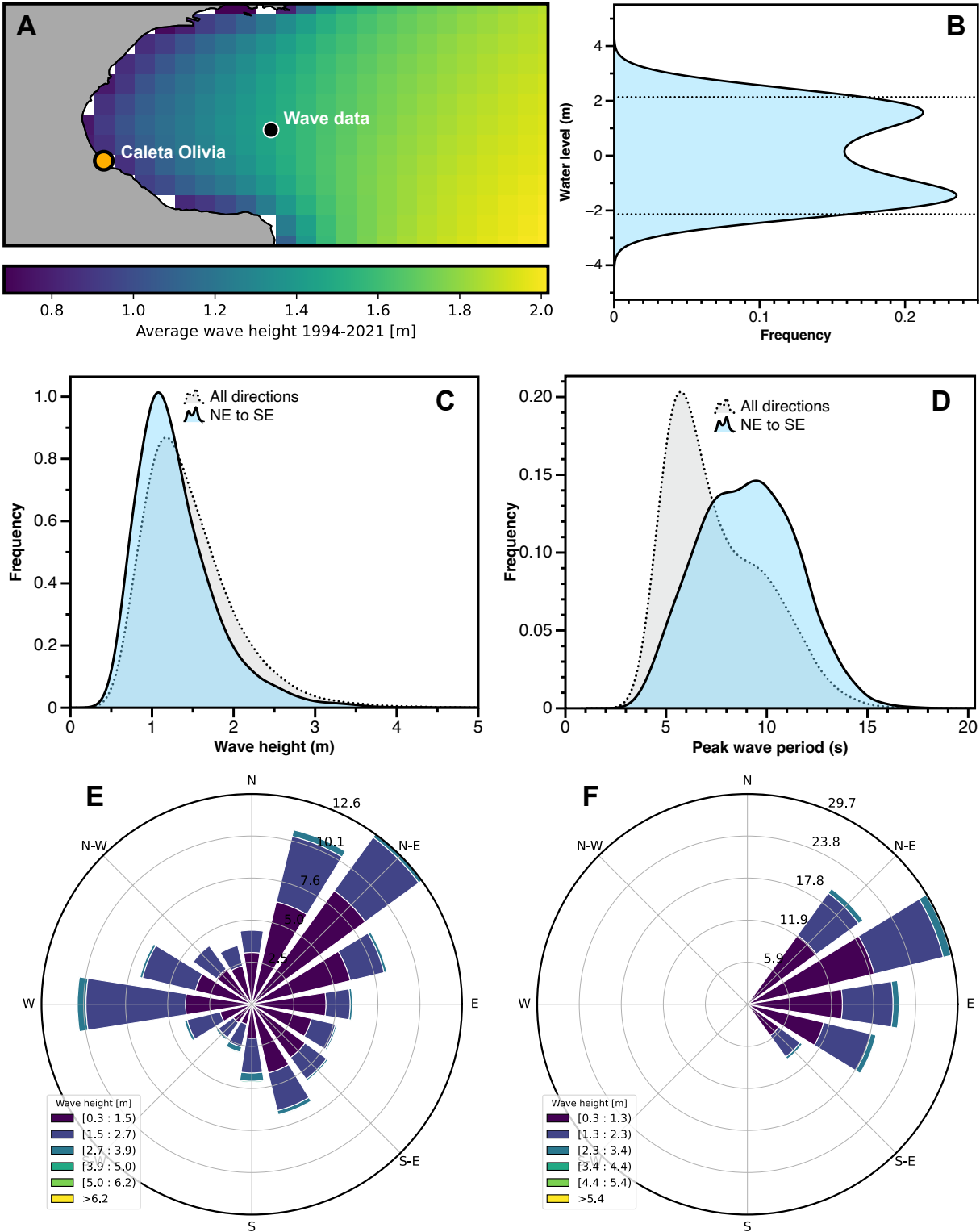


Figure 4: A) Average significant wave height in the study area extracted from the Copernicus Marine Environment Monitoring Service (CMEMS) WAVEReanalysis (WAVERYYS, Law-Chune et al., 2021), with indication of points where tidal (orange) and wave (black) data were extracted. B) Smoothed histogram plot of tidal data extracted from the FES2014 model at Caleta Olivia (Lyard et al., 2021; Carrere et al., 2016). The horizontal lines represent MHHW and MLLW calculated by the the "CO-OPS Tidal Analysis DatumCalculator" (Licate et al., 2017). C) and D) Smmoothed histogram plots of, respectively, significant wave height and period for all directions (gray shade) or only perpendicular to the coast (NE to SE, cyan shade). E and F) Direction of significant waves for, respectively, all waves and waves perpendicular to the coast.

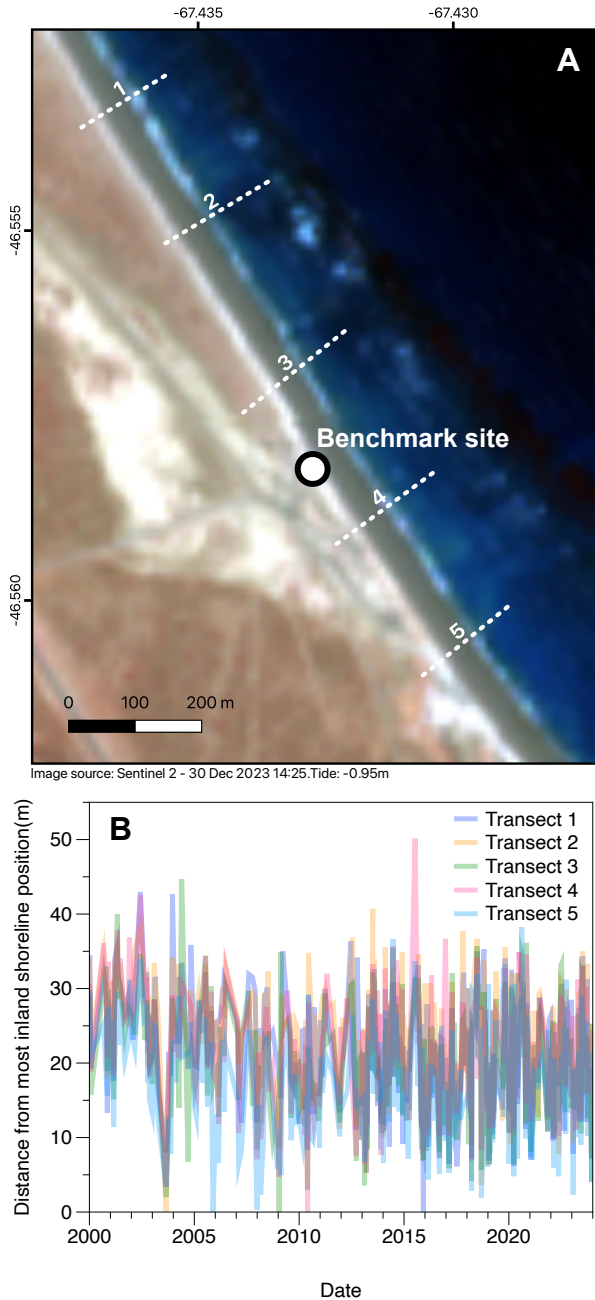


Figure 5: A) Satellite image of the study area from Sentinel2, with transects 1-5 analysed in CoastSat and location of the benchmark site. B) Results of the CoastSat shoreline variation analysis (corrected for tidal range), showing the shoreline variation from the distance from the most inland position detected at each transect over the period 2000-2023.

357 4.2.3 Step 3 - Runup calculation

358 In the last step of our workflow, we use wave, tidal data, and
 359 the beach slope calculated above to simulate R_2 . There are
 360 several approaches and several empirical formulas that have
 361 been proposed to calculate R_2 on sandy beaches (see a recent
 362 review by Gomes da Silva et al., 2020). The most common
 363 among these were compiled in the *py-wave-runup* tool (Leaman

et al., 2020). Using this tool, we run nine models that require as
 input significant wave height, period and beach slope (Holman,
 1986; Ruggiero et al., 2001; Stockdon et al., 2006; Nielsen, 2009;
 Senechal et al., 2011; Vousdoukas et al., 2012; Atkinson et al.,
 2017; Passarella et al., 2018; Beuzen et al., 2019). We run these
 models on the subset of the wave dataset shown in Figure 4 E,
 that corresponds to waves with direction perpendicular to the
 coast (at our benchmark site, those with orientation NE-SE).
 We also consider only the waves hitting the coast when the
 tide is equal or above mean sea level, as we assume that waves
 hitting below MSL would produce ephemeral landforms, that
 are usually re-eroded within one or two tidal cycles.

We test the results of these models against the height of the swash
 zone measured at the time of our survey (0.55 m, Figure 2 B).
 The modelled runup (corrected by the tide at the time of survey)
 shows good agreement with the observed reach of waves during
 the survey (Figure 6 A). Also the other morphological elements
 we observed on the modern beach fall within the probability
 density distribution of the modelled runup (Figure 6 B).

The modern runup is representative of the wave and tidal condi-
 tions over the last 30 years. Over an interglacial, it is possible
 that the same storm measured in the modern happened at differ-
 ent stages of the tide, or with a slightly different beach slope.
 To account for this possibility, we create a synthetic dataset
 composed of one million different conditions of waves, tides
 and beach slope. The synthetic dataset is created by randomly
 sampling a pair of wave height and period, one tidal level above
 MSL and one value of beach slope (β) from a normal random
 distribution with average 0.1 and standard deviation 0.01. We
 then use this dataset as input to the 9 runup models as described
 above, obtaining the probability distribution shown in Figure 6
 C.

We use this distribution to derive the indicative meaning of
 the storm beach ridge in the area, assuming that it would form
 between the 1st and 99th percentiles of the calculated wave
 runup. Under this assumption, the upper and lower limits of
 the indicative range would be, respectively, 4.7 m and 0.9 m
 (Figure 6 C). Using these values, we calculate that paleo RSL as
 indicated by the articulated shells layer at 17.9 m (Figure 2 C)
 is 15.1 ± 1.9 m (1σ).

5 DISCUSSION

From the measurement of the modern analog, we reconstruct
 that paleo RSL at the benchmark site used in this work is $14.5 \pm$
 2 m. This is consistent with the interpretation of Unit 1, located
 below the articulated shells we used as index point, that was
 interpreted as forming in the lower intertidal / subtidal zone
 (Schellmann, 1998). The paleo RSL calculated from the beach
 ridge at this site is also confirmed by that derived from the
 paleo shore platform, which sets paleo RSL at 15.4 ± 1.1 m
 (Figure 7). There is a striking similarity between the paleo RSL
 reconstructed from the modern analog and that derived from the
 runup-based reconstructions of Lorscheid and Rovere (2019),
 Rubio-Sandoval et al. (2024) and the one used in this work
 (Figure 7).

To quantify the similarity between the paleo RSL distributions
 obtained with runup models and the one gathered from the mod-
 ern analog, we use the Kolmogorov-Smirnov test. The test

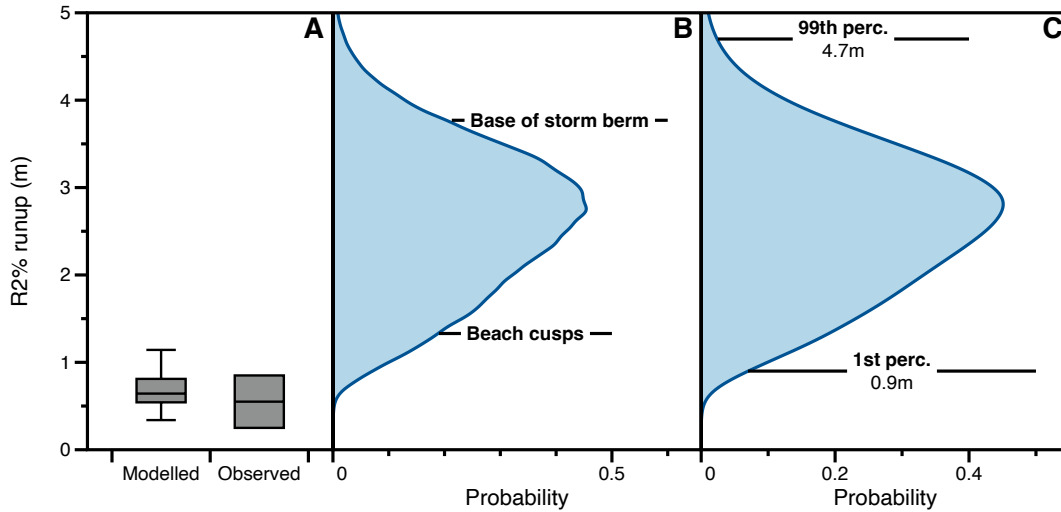


Figure 6: A) Comparison between modelled and observed swash height at the time of survey (11 Feb 2019, 15.55 PM). B) Probability density plot representing simulated 2% wave runup at the benchmark site between 1993 and 2023, for waves perpendicular to the shore and reaching the coast in tidal conditions from MSL to high tide. A breakup of this histogram into the contribution of different wave models is shown in [Supplementary Figure 4](#). C) Probability density plot representing simulated 2% wave runup at the benchmark site for the synthetic dataset described in the main text.

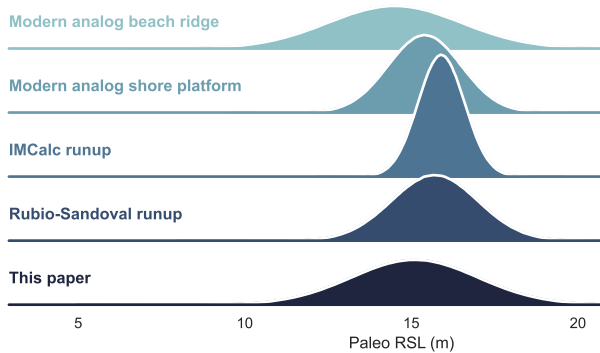


Figure 7: Comparison between paleo RSL calculated using indicative meaning estimated by the modern analog, IMCalc ([Lorscheid and Rovere, 2019](#)) and the methodology outlined in this work.

421 returns a statistic D which is the maximum difference between
 422 the empirical distribution functions of the two samples. D varies
 423 between 0 and 1, with a lower D value indicating more similar-
 424 ity. We calculate the similarity in percentage as $(1 - D) \times 100$.
 425 We calculate that the similarity between the paleo RSL calcu-
 426 lated from the modern analog and that obtained from IMCalc
 427 is 49.7%. The same comparison with the method of [Rubio-
 428 Sandoval et al. \(2024\)](#) yields a similarity score of 67.7% and
 429 with the one from the workflow presented in this study is 87.6%.
 430 Compared to previous runup-based approaches, both IMCalc
 431 ([Lorscheid and Rovere, 2019](#)) and [Rubio-Sandoval et al. \(2024\)](#)
 432 reconstruct correctly the paleo RSL at the benchmark site, but
 433 they underestimate error bars.

434 It is worth highlighting that the method proposed here is valid
 435 only if a key assumption is made: that the wave intensity and

436 tidal range were, in the area of interest, the same at the time
 437 of formation of the beach ridge as they are today. For which
 438 concerns paleo tidal ranges, models of tidal range changes in
 439 the Pleistocene are limited in time ([Wilmes et al., 2023](#)) or are
 440 constrained to a restricted geographic area ([Lorscheid et al.,
 441 2017](#)). Substantially more work on tidal range changes and on
 442 their implication on the reconstruction of paleo RSL has been
 443 done for the Holocene ([Horton et al., 2013](#); [Sulzbach et al., 2023](#);
 444 [Hill et al., 2011](#)). A global model of tidal range changes for
 445 the Pleistocene interglacials does not exist, but it would allow
 446 correcting the runup calculations for different tides at Step 2 of
 447 the workflow presented in this study.

448 Also the intensity of waves in previous interglacials (more specifi-
 449 cally in the Last Interglacial) has been widely debated, mostly
 450 on the basis of particular landforms ([Rovere et al., 2017](#); [Hearty
 451 and Tormey, 2018](#); [Rovere et al., 2018](#)). Models on the intensity
 452 and direction of storms and tropical cyclones suggest that it can-
 453 not be assumed that wave characteristics were the same between
 454 the present and the Last Interglacial ([Kaspar et al., 2007](#); [Yan
 455 et al., 2021](#); [Huan et al., 2023](#)), but models that quantify the
 456 change in significant wave height and period are still missing.

457 [Scussolini et al. \(2023\)](#) provide global models of storm surges
 458 for extreme storms in the Last Interglacial which, for the area
 459 of interest, indicate that extreme storm surge would have been
 460 higher by less than ~ 7 cm with respect to present-day ([Supple-
 461 mentary Figure 6](#)). This would not change substantially the
 462 paleo RSL calculated above. We note that, towards the Northern
 463 part of the San Jorge gulf, this assumption might not be true,
 464 and the upper limit of storm-built beach ridges would have to be
 465 corrected upwards by up to ~ 20 cm ([Supplementary Figure 6](#)).

466 It is also worth noting that, from the wave, tidal and runup data
 467 calculated by the workflow presented here, it may be possible to
 468 calculate the indicative meaning of other depositional sea-level
 469 index points, such as beach deposits of different kinds ([Figure 8](#)).

470 As an example, the general definition of beach deposits entails
 471 that they form between the ordinary berm and the depth of
 472 closure of ordinary waves (Rovere et al., 2016), which can be
 473 easily quantified from wave data and runup models (Lorscheid
 474 and Rovere, 2019), such as those used in our workflow for beach
 475 ridges.

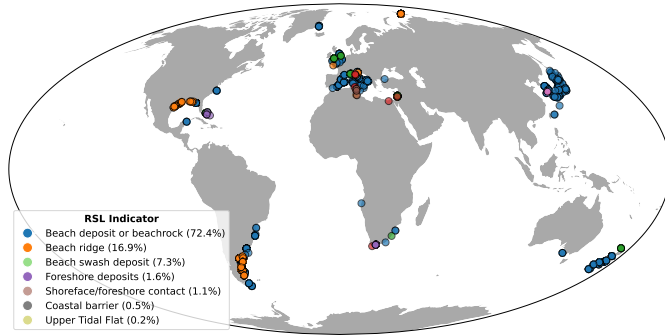


Figure 8: Map showing depositional sea-level index points in the World Atlas of Last Interglacial Shorelines (WALIS, Rovere et al., 2023). The number in parenthesis near each category in the legend indicate the frequency of each indicator within the depositional index points in WALIS, which represent ~12% of the global database.

476 6 CONCLUSIONS

477 Storm-built beach ridges are widely used, in particular along
 478 the Atlantic coasts, to reconstruct Holocene and Pleistocene
 479 sea-level changes. However, the modern analog of these land-
 480 forms, to allow the quantification of paleo RSL, is less studied
 481 and is seldom reported in the literature. Our results show that it
 482 is possible to exploit freely available satellite-derived data and
 483 models that are commonly employed to study modern coastal
 484 processes to obtain a reliable estimate of the paleo RSL associ-
 485 ated with beach ridges. With our workflow, that is entirely based
 486 on remotely sensed data, we obtain a similarity of 87.6% in com-
 487 parison with the paleo RSL calculated from modern analog data.
 488 We surmise that this workflow may be used to better quantify
 489 the indicative meaning of fossil storm beach ridges. The wave,
 490 tidal and runup data calculated in our workflow may be also
 491 employed to calculate the indicative meaning of other coastal
 492 landforms in absence of modern analog data.

493 ACKNOWLEDGMENTS

494 Tidal data used in this work were extracted from FES2014, a
 495 product by NOVELTIS, LEGOS, CLS Space Oceanography Di-
 496 vision and CNES. It is distributed by AVISO, with support from
 497 CNES (<http://www.aviso.altimetry.fr/>). Wave data
 498 was Generated using E.U. Copernicus Marine Service Informa-
 499 tion ([https://data.marine.copernicus.eu/product/
 500 GLOBAL_MULTIYEAR_WAV_001_032/description](https://data.marine.copernicus.eu/product/GLOBAL_MULTIYEAR_WAV_001_032/description)). The
 501 authors acknowledge PALSEA for useful discussions during
 502 annual meetings. PALSEA is a working group of the Inter-
 503 national Union for Quaternary Sciences (INQUA) and Past
 504 Global Changes (PAGES), which in turn received support from

the Swiss Academy of Sciences and the Chinese Academy of
 Sciences.

FUNDING

This project has received funding from the European Research
 Council (ERC) under the European Union’s Horizon 2020 re-
 search and innovation programme (grant agreement no. 802414
 to AR). EJG was funded by an International Postdoctoral Fellow-
 ship of Japan Society for the Promotion of Science, Helmholtz
 Exzellenznetzwerks “The Polar System and its Effects on the
 Ocean Floor (POSY)” and the Helmholtz Climate Initiative
 REKLIM (Regional Climate Change), a joint research project at
 the Helmholtz Association of German Research Centres (HGF),
 and also supported by the PACES II program at the Alfred
 Wegener Institute and the Bundesministerium für Bildung und
 Forschung-funded project, PalMod. SR acknowledges a fel-
 lowship by INQUA, and projects PUE-IPGP-CONICET and
 PICT2020A-1763.

AUTHORS CONTRIBUTIONS

AR had the initial idea and wrote the paper with substantial input
 from MP. AR made the code for the workflow described in the
 paper. SR, AM and PMR provided insights on local geology,
 geomorphology and paleobiology. AR, MP, SR, DDR, KRS,
 PMR and EJG participated to different field campaigns at Caleta
 Olivia, that resulted in the data used for this paper. All authors
 revised the text, giving input according to their expertise, and
 agree with its contents.

SUPPLEMENTARY INFORMATION

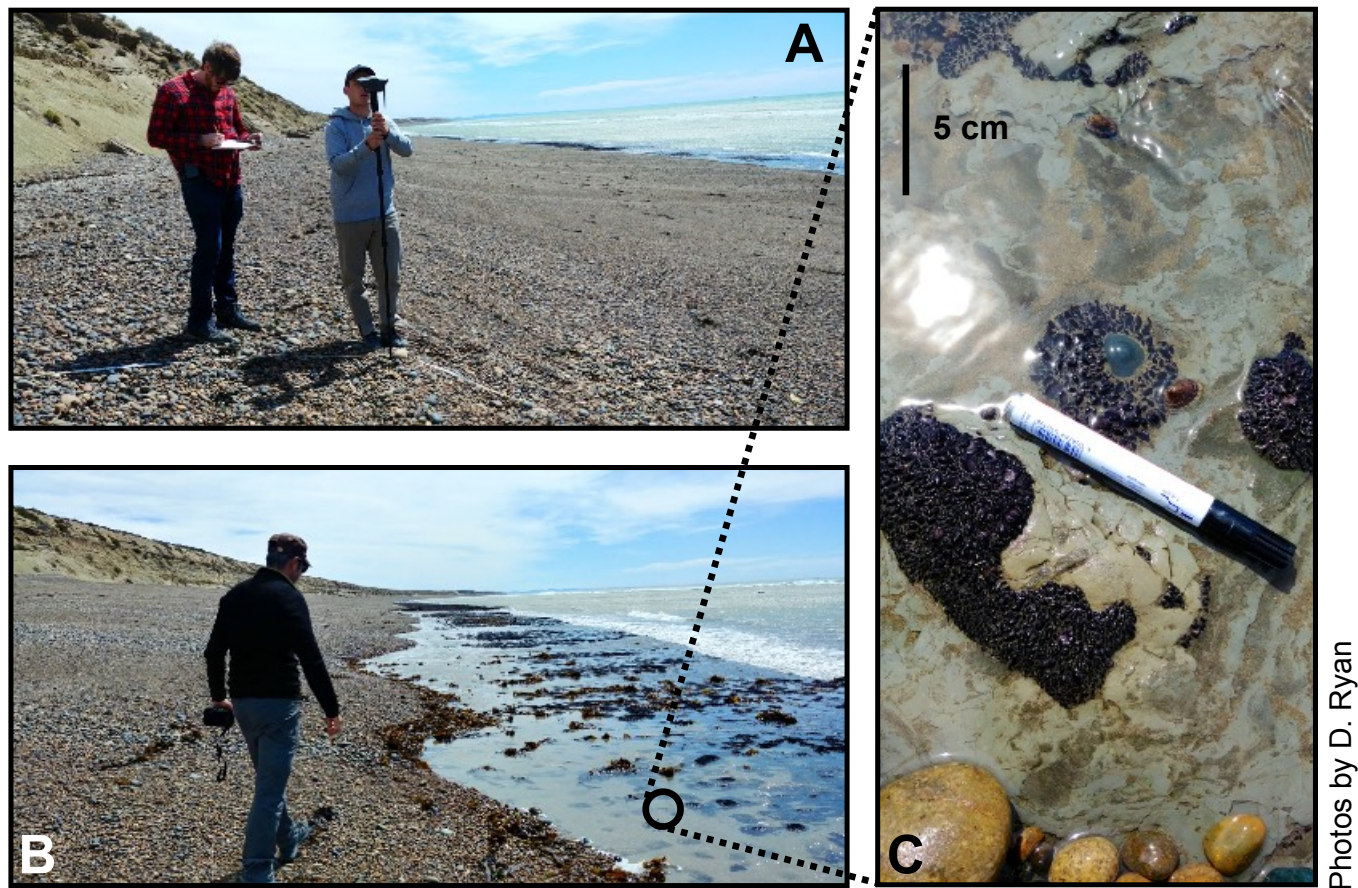
The Supplementary Information to this paper contains all the
 raw data described in this paper and the jupyter notebooks to
 reproduce the results of this work and apply the same workflow
 in other areas (Rovere, 2024).

536 REFERENCES

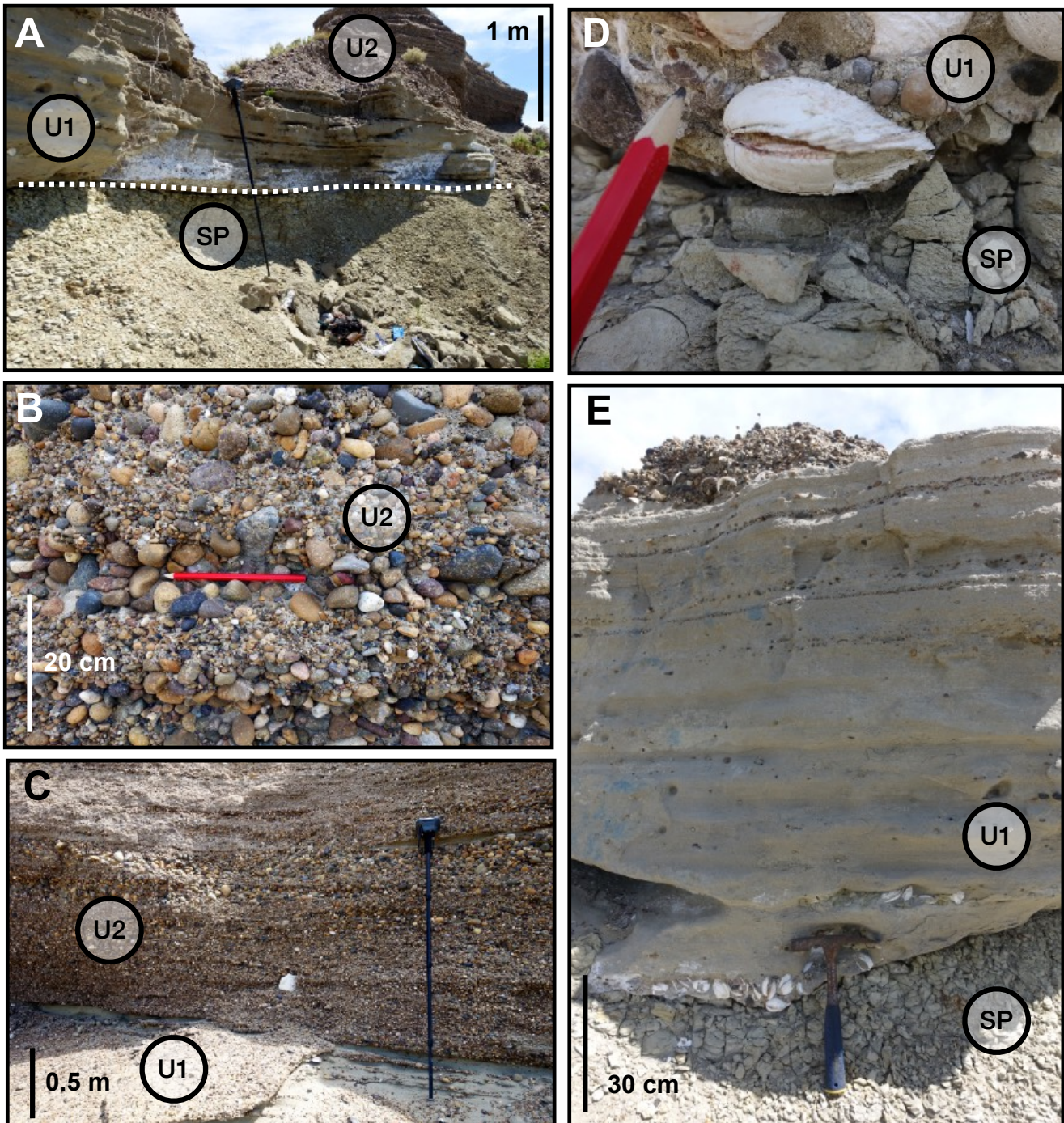
- 537 Aguirre, M. L. (2003). Late Pleistocene and Holocene palaeoenvironments in Golfo San Jorge, Patagonia: molluscan evidence. *Marine Geology* 194(1-2), 3–30. 592
- 538
- 539
- 540 Atkinson, A. L., H. E. Power, T. Moura, T. Hammond, D. P. Callaghan, and T. E. Baldock (2017). Assessment of runup predictions by empirical models on non-truncated beaches on the south-east Australian coast. *Coastal Engineering* 119, 15–31. 593
- 541
- 542
- 543
- 544
- 545 Beuzen, T., E. B. Goldstein, and K. D. Splinter (2019). Ensemble models from machine learning: an example of wave runup and coastal dune erosion. *Natural Hazards and Earth System Sciences* 19(10), 2295–2309. 594
- 546
- 547
- 548
- 549 Bird, P. (2003). An updated digital model of plate boundaries. *Geochemistry, Geophysics, Geosystems* 4(3). 595
- 550
- 551 Blanco-Chao, R., K. Pedoja, C. Witt, J. Martinod, L. Husson, V. Regard, L. Audin, M. Nexer, B. Delcaillau, M. Saillard, D. Melnick, J. F. Dumont, E. Santana, E. Navarrete, C. Martillo, M. Pappalardo, L. Ayala, J. F. Araya, A. Feal-Pérez, D. Correa, and I. Arozarena-Llopis (2014). Chapter 10 The rock coast of South and Central America. *Geological Society, London, Memoirs* 40(1), 155–191. 596
- 552
- 553
- 554
- 555
- 556
- 557
- 558 Carrere, L., F. Lyard, M. Cancet, A. Guillot, and N. Picot (2016). FES2014, a new tidal model—Validation results and perspectives for improvements, presentation to ESA Living Planet Conference. 597
- 559
- 560
- 561
- 562 Codignotto, J. (1983). Depósitos elevados y/o de acreción Pleistoceno-Holoceno en la costa Fueguino-Patagónica. In *Simposio Oscilaciones del nivel del mar durante el último hemicyclo deglacial en la Argentina*, pp. 12–26. 598
- 563
- 564
- 565
- 566 Codignotto, J. O., R. R. Kokot, and S. C. Marcomini (1992). Neotectonism and sea-level changes in the coastal zone of Argentina. *Journal of coastal research*, 125–133. 599
- 567
- 568
- 569 Darwin, C. (1846). *Geology of the Voyage of the Beagle, Under the Command of Capt. Fitzroy, RN During the Years 1832 to 1836: III*. Smith, Elder. 600
- 570
- 571
- 572 Durrant, T., M. Hemer, C. Trenham, and D. Greenslade (2013). CAWCR Wave Hindcast 1979–2010 v7. *CSIRO Data Collect*. 601
- 573
- 574 Gomes da Silva, P., G. Coco, R. Garnier, and A. H. Klein (2020). On the prediction of runup, setup and swash on beaches. *Earth-Science Reviews* 204, 103148. 602
- 575
- 576
- 577 Gowan, E. J., A. Rovere, D. D. Ryan, S. Richiano, A. Montes, M. Pappalardo, and M. L. Aguirre (2021). Last interglacial (MIS 5e) sea-level proxies in southeastern South America. *Earth System Science Data* 13(1), 171–197. 603
- 578
- 579
- 580
- 581 Hearty, P. J. and B. R. Tormey (2018). Listen to the whisper of the rocks, telling their ancient story. *Proceedings of the National Academy of Sciences* 115(13), E2902–E2903. 604
- 582
- 583
- 584 Hesp, P. (2006). Sand beach ridges: definitions and re-definition. *Journal of Coastal Research*, 72–75. 605
- 585
- 586 Hill, D. F., S. D. Griffiths, W. R. Peltier, B. P. Horton, and T. E. Törnqvist (2011). High-resolution numerical modeling of tides in the western Atlantic, Gulf of Mexico, and Caribbean Sea during the Holocene. *Journal of Geophysical Research: Oceans* 116(C10). 606
- 587
- 588
- 589
- 590
- Holman, R. (1986). Extreme value statistics for wave run-up on a natural beach. *Coastal Engineering* 9(6), 527–544. 607
- Horton, B. P., S. E. Engelhart, D. F. Hill, A. C. Kemp, D. Nikitina, K. G. Miller, and W. R. Peltier (2013). Influence of tidal-range change and sediment compaction on Holocene relative sea-level change in New Jersey, USA. *Journal of Quaternary Science* 28(4), 403–411. 608
- Huan, D., Q. Yan, and T. Wei (2023, September). Unfavorable environmental conditions for tropical cyclone genesis over the western North Pacific during the Last Interglacial based on PMIP4 simulations. *Atmospheric and Oceanic Science Letters* 16(5), 100395. 609
- Kaspar, F., T. Spanghehl, and U. Cubasch (2007, April). Northern hemisphere winter storm tracks of the Eemian interglacial and the last glacial inception. *Climate of the Past* 3(2), 181–192. 610
- Khan, N. S., B. P. Horton, S. Engelhart, A. Rovere, M. Vacchi, E. L. Ashe, T. E. Törnqvist, A. Dutton, M. P. Hijma, and I. Shennan (2019). Inception of a global atlas of sea levels since the Last Glacial Maximum. *Quaternary Science Reviews* 220, 359–371. 611
- Law-Chune, S., L. Aouf, A. Dalphinnet, B. Levier, Y. Drillet, and M. Drevillon (2021). WAVERYS: a CMEMS global wave reanalysis during the altimetry period. *Ocean Dynamics* 71, 357–378. 612
- Leaman, C., T. Beuzen, and E. B. Goldstein (2020, January). chrisleaman/py-wave-runup: v0.1.10. 613
- Lellouche, J.-M., E. Greiner, O. Le Galloudec, G. Garric, C. Regnier, M. Drevillon, M. Benkiran, C.-E. Testut, R. Bourdalle-Badie, F. Gasparin, et al. (2018). Recent updates to the Copernicus Marine Service global ocean monitoring and forecasting real-time 1/12 high-resolution system. *Ocean Science* 14(5), 1093–1126. 614
- Licate, L. A., G. Dusek, and L. Huang (2017). A comparison of datums derived from CO-OPS verified data products and Tidal Analysis Datum Calculator. 615
- Lorscheid, T., T. Felis, P. Stocchi, J. C. Obert, D. Scholz, and A. Rovere (2017, November). Tides in the Last Interglacial: insights from notch geometry and palaeo tidal models in Bonaire, Netherland Antilles. *Scientific Reports* 7(1), 16241. 616
- Lorscheid, T. and A. Rovere (2019). The indicative meaning calculator—quantification of paleo sea-level relationships by using global wave and tide datasets. *Open Geospatial Data, Software and Standards* 4, 1–8. 617
- Lyard, F. H., D. J. Allain, M. Cancet, L. Carrère, and N. Picot (2021). FES2014 global ocean tide atlas: design and performance. *Ocean Science* 17(3), 615–649. 618
- Lyell, C. (1837). *Principles of geology: being an inquiry how far the former changes of the earth's surface are referable to causes now in operation*, Volume 1. J. Kay, jun. & brother. 619
- Martínez, H., D. Molín, C. Nelson, S. E. Castro Godoy, F. Quintón Piegas Luna, H. G. Marengo, M. A. Dzendoletas, H. D. Pezzuchi, C. Parisi, J. L. A. Panza, et al. (2020). Hoja Geológica 4769-II Colonia Las Heras y Hoja Geológica 4766-I Bahía Lángara, Provincia de Santa Cruz. 620
- Martínez, S. and A. Rojas (2013). Relative sea level during the Holocene in Uruguay. *Palaeogeography, Palaeoclimatology, Palaeoecology* 374, 123–131. 621
- 622
- 623
- 624
- 625
- 626
- 627
- 628
- 629
- 630
- 631
- 632
- 633
- 634
- 635
- 636
- 637
- 638
- 639
- 640
- 641
- 642
- 643
- 644
- 645
- 646
- 647

- 648 Nielsen, P. (2009). *Coastal and estuarine processes*, Volume 29. 704
 649 World Scientific Publishing Company. 705
- 650 Otvos, E. G. (2020, April). Coastal barriers - fresh look at 706
 651 origins, nomenclature and classification issues. *Geomorphol-* 707
 652 *ogy* 355, 107000.
- 653 Pappalardo, M., M. L. Aguirre, M. Bini, I. Consoloni, E. E. 708
 654 Fucks, J. Hellstrom, I. Isola, A. Ribolini, and G. Zanchetta 709
 655 (2015). Coastal landscape evolution and sea-level change: a 710
 656 case study from Central Patagonia (Argentina). 711
- 657 Pappalardo, M., C. Baroni, M. Bini, I. Isola, A. Ribolini, M. C. 712
 658 Salvatore, and G. Zanchetta (2019). Challenges in relative 713
 659 sea-level change assessment highlighted through a case study: 714
 660 The central coast of Atlantic Patagonia. *Global and Planetary* 715
 661 *Change* 182, 103008. 716
- 662 Passarella, M., E. B. Goldstein, S. De Muro, and G. Coco (2018). 717
 663 The use of genetic programming to develop a predictor of 718
 664 swash excursion on sandy beaches. *Natural Hazards and* 719
 665 *Earth System Sciences* 18(2), 599–611. 720
- 666 Piñón, D., K. Zhang, S. Wu, and S. Cimbaro (2018). A new 721
 667 argentinean gravimetric geoid model: GEOIDEAR. In *Inter-* 722
 668 *national Symposium on Earth and Environmental Sciences* 723
 669 *for Future Generations: Proceedings of the IAG General As-* 724
 670 *sembly, Prague, Czech Republic, June 22-July 2, 2015*, pp. 725
 671 53–62. Springer.
- 672 Ramos, V. A. and M. C. Ghiglione (2008). Tectonic evolu- 726
 673 tion of the Patagonian Andes. *Developments in quaternary* 727
 674 *sciences* 11, 57–71. 728
- 675 Ribal, A. and I. R. Young (2019). 33 years of globally cali- 729
 676 brated wave height and wind speed data based on altimeter 730
 677 observations. *Scientific data* 6(1), 77. 731
- 678 Ribolini, A., M. Bini, I. Consoloni, I. Isola, M. Pappalardo, 732
 679 G. Zanchetta, E. Fucks, L. Panzeri, M. Martini, and F. Terrasi 733
 680 (2014). Late-pleistocene wedge structures along the patago- 734
 681 nian coast (argentina): chronological constraints and palaeo- 735
 682 environmental implications. *Geografiska Annaler: Series A,* 736
 683 *Physical Geography* 96(2), 161–176. 737
- 684 Richiano, S., M. L. Aguirre, and L. Giachetti (2021). Bioerosion 738
 685 on marine Quaternary gastropods from the southern Golfo San 739
 686 Jorge, Patagonia, Argentina: What do they tell us? *Journal of* 740
 687 *South American Earth Sciences* 107, 103106. 741
- 688 Rostami, K., W. Peltier, and A. Mangini (2000). Quaternary 742
 689 marine terraces, sea-level changes and uplift history of Patag- 743
 690 onia, Argentina: comparisons with predictions of the ICE-4G 744
 691 (VM2) model of the global process of glacial isostatic adjust- 745
 692 ment. *Quaternary Science Reviews* 19(14-15), 1495–1525.
- 693 Rovere, A. (2021, August). GPS-Utilities ver. 1.0. 746
- 694 Rovere, A. (2024, July). Beach-ridges-runup: Pre-review ver- 747
 695 sion. 748
- 696 Rovere, A., E. Casella, D. L. Harris, T. Lorscheid, N. A. K. Nan- 749
 697 dasena, B. Dyer, M. R. Sandstrom, P. Stocchi, W. J. D’Andrea, 750
 698 and M. E. Raymo (2017, October). Giant boulders and Last In- 751
 699 terglacial storm intensity in the North Atlantic. *Proceedings* 752
 700 *of the National Academy of Sciences* 114(46), 201712433. 753
 701 Publisher: National Academy of Sciences. 754
- 702 Rovere, A., E. Casella, D. L. Harris, T. Lorscheid, N. A. K. Nan- 755
 703 dasena, B. Dyer, M. R. Sandstrom, P. Stocchi, W. J. D’Andrea, 756
 and M. E. Raymo (2018). Reply to Hearty and Tormey: Use 757
 the scientific method to test geologic hypotheses, because 758
 rocks do not whisper. *Proceedings of the National Academy*
of Sciences, 201800534.
- Rovere, A., M. E. Raymo, M. Vacchi, T. Lorscheid, P. Stocchi, 708
 L. Gómez-Pujol, D. L. Harris, E. Casella, M. J. O’Leary, and 709
 P. J. Hearty (2016). The analysis of Last Interglacial (MIS 710
 5e) relative sea-level indicators: Reconstructing sea-level in a 711
 warmer world. *Earth-Science Reviews* 159, 404–427. 712
- Rovere, A., D. D. Ryan, M. Vacchi, A. Dutton, A. R. Simms, 713
 and C. V. Murray-Wallace (2023). The World Atlas of Last 714
 Interglacial Shorelines (version 1.0). *Earth System Science* 715
Data 15(1), 1–23. 716
- Rubio-Sandoval, K., D. D. Ryan, S. Richiano, L. M. Giachetti, 717
 A. Hollyday, J. Bright, E. J. Gowan, M. Pappalardo, J. Auster- 718
 mann, D. Kaufman, et al. (2024). Quaternary and Pliocene 719
 sea-level changes at Camarones, central Patagonia, Argentina. 720
EarthArXiv eprints, X5X11H. 721
- Ruggiero, P., P. D. Komar, W. G. McDougal, J. J. Marra, and 722
 R. A. Beach (2001). Wave runup, extreme water levels and 723
 the erosion of properties backing beaches. *Journal of coastal* 724
research, 407–419. 725
- Ryan, W. B. F., S. M. Carbotte, J. O. Coplan, S. O’Hara, 726
 A. Melkonian, R. Arko, R. A. Weisell, V. Ferrini, A. Good- 727
 willie, F. Nitsche, J. Bonczkowski, and R. Zemsky (2009). 728
 Global Multi-Resolution Topography synthesis. *Geochem-* 729
istry, Geophysics, Geosystems 10(3). 730
- Saha, S., S. Moorthi, H.-L. Pan, X. Wu, J. Wang, S. Nadiga, 731
 P. Tripp, R. Kistler, J. Woollen, D. Behringer, et al. (2010). 732
 The NCEP climate forecast system reanalysis. *Bulletin of the* 733
American Meteorological Society 91(8), 1015–1058. 734
- Schellmann, G. (1998). *Jungkänozoische Landschaftsgeschichte* 735
Patagoniens (Argentinien): andine Vorlandvergletscherungen, 736
Talentwicklung und marine Terrassen. 1. Auflage, Essen: 737
 Klartext, 1998. 738
- Schellmann, G. and U. Radtke (2000). ESR dating stratigraphi- 739
 cally well-constrained marine terraces along the Patagonian 740
 Atlantic coast (Argentina). *Quaternary International* 68, 261– 741
 273. 742
- Schellmann, G. and U. Radtke (2003). Coastal terraces and 743
 Holocene sea-level changes along the Patagonian Atlantic 744
 coast. *Journal of Coastal Research*, 983–996. 745
- Scussolini, P., J. Dullaart, S. Muis, A. Rovere, P. Bakker, 746
 D. Coumou, H. Renssen, P. J. Ward, and J. C. J. H. Aerts 747
 (2023). Modeled storm surge changes in a warmer world: the 748
 Last Interglacial. *Climate of the Past* 19(1), 141–157. 749
- Senechal, N., G. Coco, K. R. Bryan, and R. A. Holman (2011). 750
 Wave runup during extreme storm conditions. *Journal of* 751
Geophysical Research: Oceans 116(C7). 752
- Shennan, I. (1986). Flandrian sea-level changes in the Fenland. 753
 II: Tendencies of sea-level movement, altitudinal changes, and 754
 local and regional factors. *Journal of Quaternary Science* 1(2), 755
 155–179. 756
- Shennan, I. (2015). Handbook of sea-level research: framing 757
 research questions. *Handbook of sea-level research*, 3–25. 758

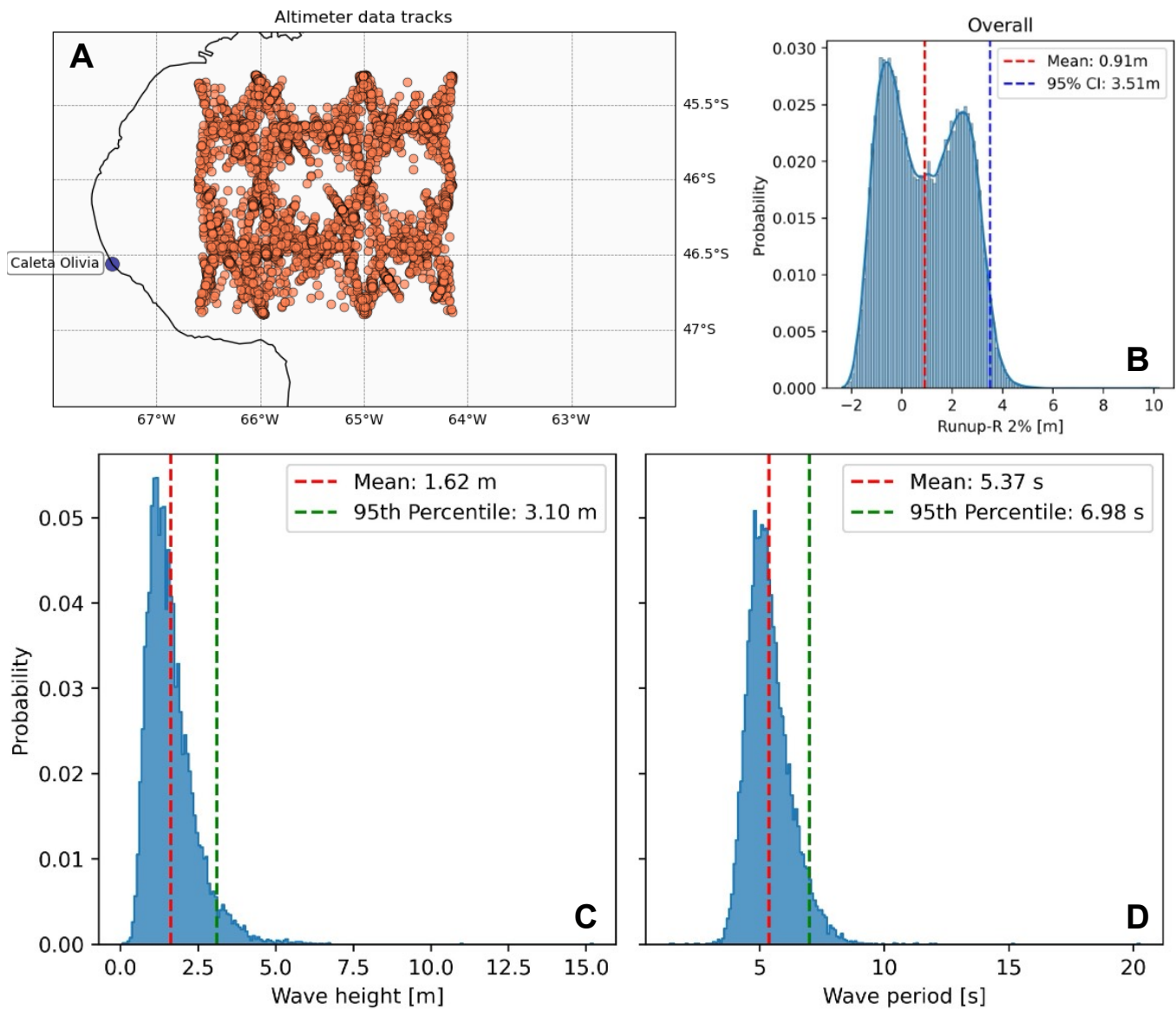
- 759 Smith, C., T. Salles, and A. Vila-Concejo (2020). RADWave:
760 Python code for ocean surface wave analysis by satellite radar
761 altimeter. *Journal of Open Source Software* 5(47), 2083.
- 762 Stockdon, H. F., R. A. Holman, P. A. Howd, and A. H. Sallenger
763 (2006). Empirical parameterization of setup, swash, and
764 runup. *Coastal Engineering* 53(7), 573–588.
- 765 Styron, R. (2019, August). GEMScienceTools/gem-global-
766 active-faults: First release of 2019.
- 767 Sulzbach, R., V. Klemann, G. Knorr, H. Dobsław, H. Düm-
768 pelmann, G. Lohmann, and M. Thomas (2023, May). Evo-
769 lution of Global Ocean Tide Levels Since the Last Glacial
770 Maximum. *Paleoceanography and Paleoclimatology* 38(5),
771 e2022PA004556.
- 772 Sunamura, T. (1992). *Geomorphology of rocky coasts*, Volume 3.
773 Wiley.
- 774 Tamura, T. (2012, September). Beach ridges and prograded
775 beach deposits as palaeoenvironment records. *Earth-Science*
776 *Reviews* 114(3-4), 279–297.
- 777 Taylor, M. and G. W. Stone (1996). Beach-ridges: a review.
778 *Journal of Coastal Research*, 612–621.
- 779 Tolman, H. L. et al. (2009). User manual and system docu-
780 mentation of WAVEWATCH III TM version 3.14. *Technical note*,
781 *MMAB contribution* 276(220).
- 782 US Geological Survey, E. H. P. (2017). Advanced National
783 Seismic System (ANSS) comprehensive catalog of earthquake
784 events and products: Various.
- 785 Van de Plassche, O. (2013). *Sea-level Research: a Manual for*
786 *the Collection and Evaluation of Data*. Springer.
- 787 Vos, K., M. D. Harley, K. D. Splinter, A. Walker, and I. L. Turner
788 (2020). Beach Slopes From Satellite-Derived Shorelines.
789 *Geophysical Research Letters* 47(14), e2020GL088365.
- 790 Vos, K., K. D. Splinter, M. D. Harley, J. A. Simmons, and I. L.
791 Turner (2019). CoastSat: A Google Earth Engine-enabled
792 Python toolkit to extract shorelines from publicly available
793 satellite imagery. *Environmental Modelling & Software* 122,
794 104528.
- 795 Vousedoukas, M. I., D. Wziatek, and L. P. Almeida (2012).
796 Coastal vulnerability assessment based on video wave run-
797 up observations at a mesotidal, steep-sloped beach. *Ocean*
798 *Dynamics* 62, 123–137.
- 799 Wilmes, S., V. K. Pedersen, M. Schindelegger, and J. A. M.
800 Green (2023, November). Late Pleistocene Evolution of
801 Tides and Tidal Dissipation. *Paleoceanography and Paleocli-*
802 *matology* 38(11), e2023PA004727.
- 803 Yan, Q., R. Korty, T. Wei, and N. Jiang (2021, June). A West-
804 ward Shift in Tropical Cyclone Potential Intensity and Genesis
805 Regions in the North Atlantic During the Last Interglacial.
806 *Geophysical Research Letters* 48(12).
- 807 Zanchetta, G., I. Consoloni, I. Isola, M. Pappalardo, A. Ribolini,
808 M. Aguirre, E. Fucks, I. Baneschi, M. Bini, L. Ragaini, et al.
809 (2012). New insights on the Holocene marine transgression
810 in the Bahía Camarones (Chubut, Argentina). *Italian Journal*
811 *of Geosciences* 131(1), 19–31.



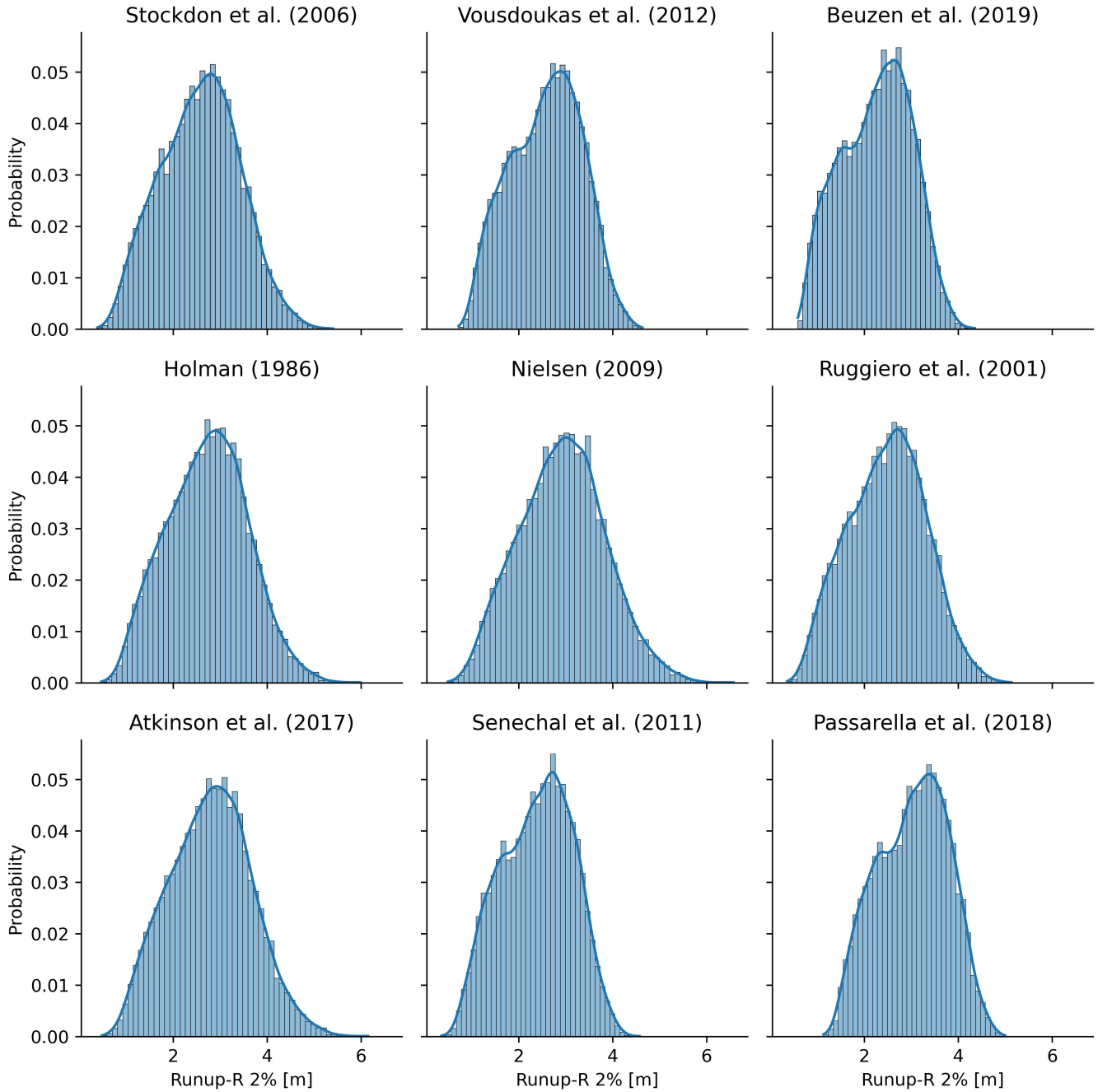
Supplementary Figure 1: Details of the modern beach at the benchmark site (Figure 2). A) view of the modern storm berm. B) lower part of the beach, with the exposed shore platform at low tide. C) detail of the shore platform, with encrusting organisms living on it.



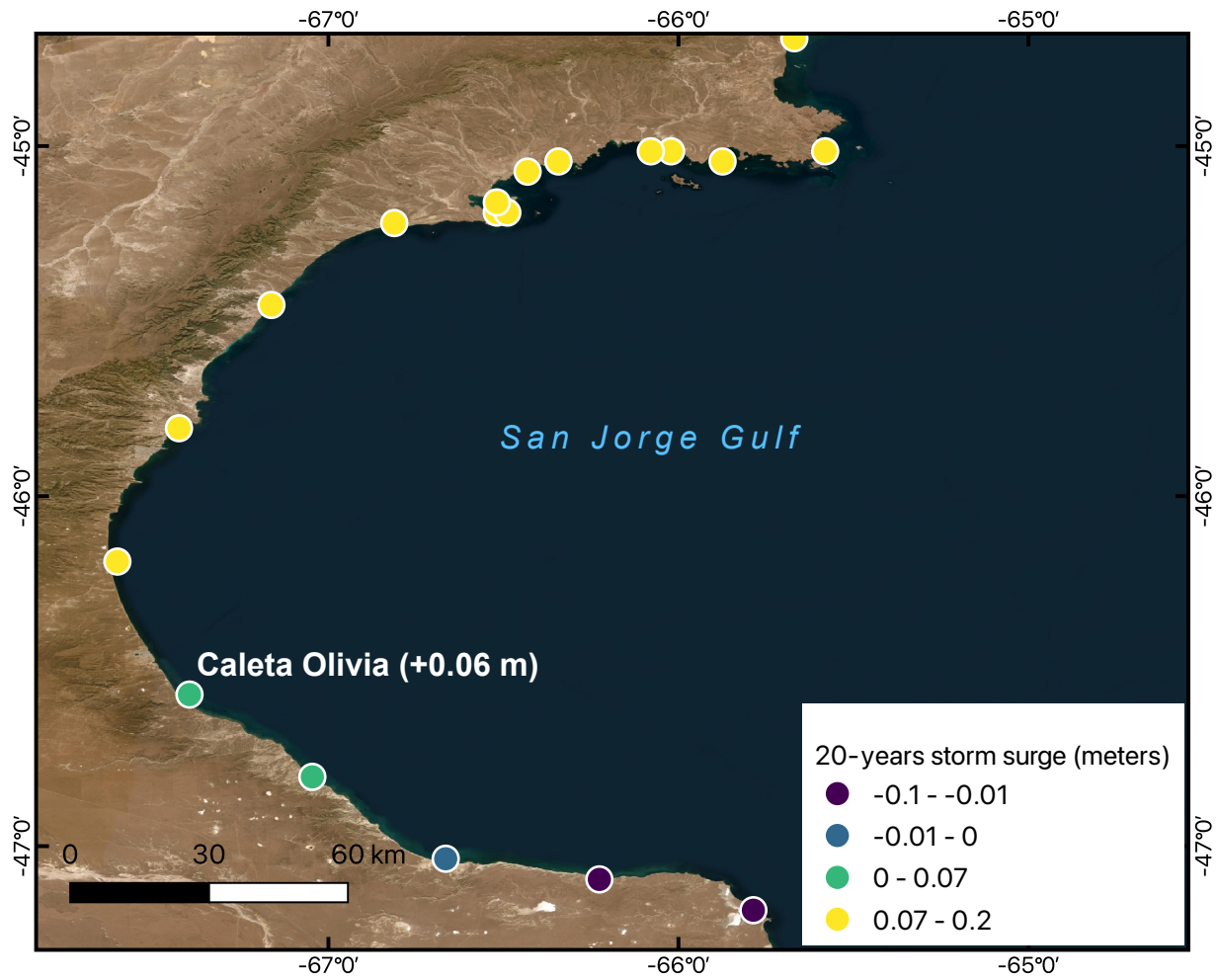
Supplementary Figure 2: Results of the runup calculations, divided by model employed, for waves perpendicular to the shore reaching the coast in tidal conditions above MSL.



Supplementary Figure 3: A) satellite altimetry data tracks exported by the RADWave software. B) Wave runup calculated at Caleta Olivia with the approach of [Rubio-Sandoval et al. \(2024\)](#). C) and D) respectively wave height and period extracted from the satellite altimetry data.



Supplementary Figure 4: Results of the different runup models used in this work. Only the runup values above MSL are shown here.



Supplementary Figure 5: Annual anomalies (Last Interglacial minus Present Interglacial) in sea level extremes at the 20-year return period in the San Jorge Gulf (Scussolini et al., 2023). Background imagery from ESRI ArcGIS Pro (World Imagery), source: Earthstar Geographics (TerraColor NextGen)